INTERNATIONAL JOURNAL FOR NUMERICAL METHODS IN FLUIDS
*Int. J. Numer. Meth. Fluids* 2003; **41**:905–930 (DOI: 10.1002/fld.473)

# Numerical simulation and experimental visualization of the influence of the deformation frequency of a radially deforming circular cylinder impulsively started on cylinder wake

S. Hanchi[1], H. Oualli[1], R. Askovic[2,*,†] and A. Bouabdallah[3]

[1] *Laboratory of Fluid Mechanics, Military Polytechnic School, BP 17, Bordj-el-Bahri, 16111 W. Algiers, Algeria*
[2] *Laboratory of Mechanics and Energetics, University of Valenciennes, France*
[3] *Institute of Physics, University of Bab-Ezzouar, Alger, Algeria*

SUMMARY

A periodic superimposed motion may notably influence the flow structure and the development of the convective heat transfer relative to non-deformable case. In particular, a radial deformation of a circular cylinder, may cause a possible synchronization with the cylinder wake, which is itself periodic when Vortex Street takes place. This synchronization phenomenon, often called 'lock-in', may cause undesirable effects, but may also constitute a way of controlling the wake development.

Body deformability may be used as wake control device that would favourably affect the interplay of primary and secondary vorticities, thus reducing the drag coefficient. These numerical and experimental studies are done herein for a Reynolds number equal to 23500. The problem is resolved by using the Navier–Stokes equations in the vorticity-stream function form. The vorticity transport equation is solved by a second-order finite difference method in both directions of the domains. The Poisson equation for the stream-function is solved by a SOR method. The advance in time is achieved by a second-order Adams–Bashforth scheme. The effect of turbulence is represented by eddy viscosity $v_t$, which is determined by a sub-grid-scale model. In the present study, we use a Smagorinsky model.


KEY WORDS: numerical simulation; experimental visualization; deformable cylinder; lock-in

## 1. INTRODUCTION

In the case where the cylinder is free from superimposed motion, but flexibly attached, the fluctuating force associated with the periodic shedding of vortices may cause the cylinder to oscillate if the damping of the system is sufficiently small. This phenomenon, known as 'self-exited' or 'induced-vibrations', has important practical consequences, often causing damage in industrial structures, because of the possibility of corresponding large amplitude values which

* Correspondence to: R. Askovic, Laboratoire de Mecanique et d'Energetique, Université de Valenciennes, Le Mont Hony, 59313 Valenciennes Cedex 9, France.
† E-mail: radomir.askovic@univ-valenciennes.fr

*Received 20 April 2002*
*Revised 16 October 2002*

may attain several cylinder diameters if the aerodynamic forces come into resonance with the eigenfrequencies of the cylinder [1].

In most experimental arrangements, especially in air because of its small density, the cylinder appears to oscillate in a direction transverse to the incident flow. Furthermore, if the free stream velocity is such that it induces a vortex shedding locks on the cylinder frequency, then the vortex configuration in the wake may be clearly modified compared with that of a stationary cylinder. In particular, at synchronization, besides the fact that the shedding frequency is shifted due to its capture by the natural body frequency, oscillations induce a clear coupling of the flow along the span of the body [2].

In the transition domain $150 < Re < 350$, slantwise vortex shedding is replaced by parallel vortex [3], delaying the decay of vortices into turbulent ones. Consequently, the wake is maintained laminar for a larger distance and for a greater range of the Reynolds Number.

## 2. BASIC EQUATIONS

Consider the unsteady flow past a circular cylinder whose radius (of initial value $a_0$) deforms uniformly with a sinusoidal function of deformability, started impulsively at the same time into rectilinear motion, with a constant velocity $U_\infty$, in a 2D viscous incompressible fluid flow initially at rest. In the case of a constant physical properties $\rho$ and $\mu$ of the fluid (this condition is satisfied even by air with a good agreement, when the velocity of the flow in less than 50 m/s and the differences of the temperature do not exceed 50 K), the unsteady Navier–Stokes equations in stream function and vorticity formulation for the flow past a circular cylinder can be written in polar co-ordinates as:

$$\frac{\partial \omega}{\partial t} = \frac{\omega}{1+f}\frac{\partial f}{\partial t} + \frac{k^{-1}(\frac{\partial k}{\partial \xi})^{-1}}{1+f}\left[\frac{\partial \omega}{\partial \xi}\frac{\partial \tilde{\psi}}{\partial \theta} - \frac{\partial \omega}{\partial \theta}\frac{\partial \tilde{\psi}}{\partial \xi}\right] + \frac{1}{1+f}\left(\frac{2}{R_e} + \frac{2}{R_{et}}\right) \times \left(\left(\frac{\partial k}{\partial \xi}\right)^{-2}\frac{\partial^2 \omega}{\partial \xi^2} + k^{-2}\frac{\partial^2 \omega}{\partial \theta^2} + \left(k^{-1}\left(\frac{\partial k}{\partial \xi}\right)^{-1} - \left(\frac{\partial^2 k}{\partial \xi^2}\right)\left(\frac{\partial k}{\partial \xi}\right)^{-3}\right)\frac{\partial \omega}{\partial \xi}\right) \tag{1}$$

$$\omega = \left(\frac{\partial k}{\partial \xi}\right)^{-2}\left(\frac{\partial^2 \tilde{\psi}}{\partial \xi^2}\right) + k^{-2}\left(\frac{\partial^2 \tilde{\psi}}{\partial \theta^2}\right) + \left(k^{-1}\left(\frac{\partial k}{\partial \xi}\right)^{-1} - \left(\frac{\partial^2 k}{\partial \xi^2}\right)\left(\frac{\partial k}{\partial \xi}\right)^{-3}\right)\frac{\partial \omega}{\partial \xi} \tag{2}$$

Here the stream function is defined by

$$u_1 = -\frac{1}{r_1}\frac{\partial \psi_1}{\partial \theta} \quad \text{and} \quad v_1 = \frac{\partial \psi_1}{\partial r_1} \tag{3}$$

the only non-zero component of the vorticity $\varpi$ is given by

$$\varpi = \frac{1}{r_1}\left(\frac{\partial}{\partial r_1}(v_1 r_1) - \frac{\partial u_1}{\partial \theta}\right) \tag{4}$$

 

and the non-dimensional quantities are given by

$$\frac{a}{a_0} = f, \quad f = (1 + A\sin(2\pi\Omega t)), \quad r = \frac{r_1}{a} = k(\xi) = \alpha e^{\xi} + \beta, \quad R_e = \frac{2U_\infty a}{\nu}, \quad t = \frac{t_1 U_\infty}{a_0}$$

$$\tilde{\psi} = \frac{\psi_1}{U_\infty a}, \quad \omega = \frac{\varpi a}{U_\infty}, \quad R_{et} = \frac{2U_\infty a}{\nu_t}, \quad \beta = 1 - \alpha, \quad 0 < \alpha = C_{te} < 1 \tag{5}$$

The effect of turbulence is represented by eddy viscosity $\nu_t$, which is determined by a subgrid scale model. In the present study, we use the Smagorinsky model:

$$\nu_t = (C_s \Delta)^2 \sqrt{2 S_{ij} S_{ij}} \tag{6}$$

where $C_s$ is the Smagorinsky constant, $\Delta$ is the length scale (taken here to be the local mesh size), and $S_{ij}$ is the strain rate tensor.

### 2.1. Initial conditions

The cylinder, as is suddenly started from rest, has the following initial conditions:

$$\tilde{\psi} = 0 \qquad \text{and} \qquad \omega = 0 \quad \text{at } t = 0 \tag{7}$$

### 2.2. Boundary conditions

*2.2.1. For $\xi = 0$.* The cylinder, being radially deformable, has the following velocity components at the wall:

$$u_1 = \frac{\partial a}{\partial t_1} \quad \text{and} \quad v_1 = 0 \tag{8}$$

i.e. taking into account (3)

$$v_1 = \frac{\partial \psi_1}{\partial r_1} = 0 \rightarrow \psi_1 \text{ is independent of } r_1$$

i.e $\tilde{\psi}$ is independent of $\xi$.

$$u_1 = -\frac{1}{r_1}\frac{\partial \psi_1}{\partial \theta} = \frac{\partial a}{\partial t_1} \quad \text{whence} \quad \tilde{\psi} = -k(0)\frac{\partial f}{\partial t}\theta \tag{9}$$

where $k(0)$ is the value of $k(\xi)$ for $\xi = 0$ ($k(0) = \alpha + \beta = 1$).

It results from the previous equation that $\tilde{\psi}$ is a non-uniform function on the surface of the cylinder. Hence, a uniform function $\psi$ is introduced by

$$\psi = \tilde{\psi} + k(0)\frac{\partial f}{\partial t}\theta \tag{10}$$

*2.2.2. For $\xi \to \infty$.* The stream function of the flow past a circular deformable cylinder is well-known:

$$\tilde{\psi} = \left(k(\xi_\infty) - \frac{1}{k(\xi_\infty)}\right)\sin(\theta) - \frac{\theta}{k(\xi_\infty)}\frac{\partial f}{\partial t} \tag{11}$$

 

where $k(\xi\infty)$ is the value of $k(\xi)$ corresponding to the maximum radius of the computational domain.

By introducing the uniform stream function (10), the boundary condition is determined by

$$\psi = \left(k(\xi_\infty) - \frac{1}{k(\xi_\infty)}\right)\sin(\theta) - \frac{\theta}{k(\xi_\infty)}\frac{\partial f}{\partial t} + k(0)\frac{\partial a}{\partial t}\theta \tag{12}$$

*2.2.3. New system to resolve.* The new system to resolve is determined by

$$\frac{\partial \omega}{\partial t} = \frac{\omega}{1+f}\frac{\partial f}{\partial t} + G \tag{13}$$

$$\omega = \left(\frac{\partial k}{\partial \xi}\right)^{-2}\left(\frac{\partial^2 \psi}{\partial \xi^2}\right) + k^{-2}\left(\frac{\partial^2 \psi}{\partial \theta^2}\right) + \left(k^{-1}\left(\frac{\partial k}{\partial \xi}\right)^{-1} - \left(\frac{\partial^2 k}{\partial \xi^2}\right)\left(\frac{\partial k}{\partial \xi}\right)^{-3}\right)\frac{\partial \omega}{\partial \xi} \tag{14}$$

where

$$G = \frac{k^{-1}\left(\dfrac{\partial k}{\partial \xi}\right)^{-1}}{1+f} - \left[\frac{\partial \omega}{\partial \xi}\left(\frac{\partial \psi}{\partial \theta} - k(0)\frac{\partial f}{\partial t}\right) - \frac{\partial \omega}{\partial \theta}\frac{\partial \psi}{\partial \xi}\right] + \frac{1}{1+f}\left(\frac{2}{R_e} + \frac{2}{R_{et}}\right)$$
$$\times \left(\left(\frac{\partial k}{\partial \xi}\right)^{-2}\frac{\partial^2 \omega}{\partial \xi^2} + k^{-2}\frac{\partial^2 \omega}{\partial \theta^2} + \left(k^{-1}\left(\frac{\partial k}{\partial \xi}\right)^{-1} - \left(\frac{\partial^2 k}{\partial \xi^2}\right)\left(\frac{\partial k}{\partial \xi}\right)^{-3}\right)\frac{\partial \omega}{\partial \xi}\right) \tag{15}$$

with the new boundary conditions

$$\psi = 0 \quad \text{for } \xi = 0 \tag{16}$$

$$\psi = \left(k(\xi_\infty) - \frac{1}{k(\xi_\infty)}\right)\sin(\theta) - \frac{\theta}{k(\xi_\infty)}\frac{\partial f}{\partial t} + k(0)\frac{\partial a}{\partial t}\theta \quad \text{for } \xi \to \infty \tag{17}$$

$$\frac{\partial \omega}{\partial t} = \frac{\omega}{1+f}\frac{\partial f}{\partial t} + \frac{k^{-1}\left(\dfrac{\partial k}{\partial \xi}\right)^{-1}}{1+f}\left[\frac{\partial \omega}{\partial \xi}\left(\frac{\partial \psi}{\partial \theta} - k(0)\frac{\partial f}{\partial t}\right) - \frac{\partial \omega}{\partial \theta}\frac{\partial \psi}{\partial \xi}\right] \quad \text{for } \xi \to \infty \tag{18}$$

## 3. FORCES ON THE BODY

The drag force may be computed as the sum of the pressure drag $\mathbf{f}_p$ and the friction drag $\mathbf{f}_f$. The pressure drag can be determined from the vorticity flux on the cylinder surface as

$$\mathbf{F}_p = -\int_0^{2\pi}\left(\frac{2}{R_e}\frac{\partial \omega}{\partial \xi} + \left(\frac{\partial \psi}{\partial \theta} - \frac{1}{a_0}\frac{\partial a}{\partial t}\right)\omega\right)\mathbf{e}_\theta \, d\theta \tag{19}$$

 

while the friction drag may be computed from the vorticity on the cylinder surface as

$$\mathbf{F}_{\mathrm{f}} = \int_0^{2\pi} \left(\frac{2\omega}{R_{\mathrm{e}}}\right) \mathbf{e}_\theta \, \mathrm{d}\theta \tag{20}$$

Hence, the total drag force on the body follows

$$\mathbf{F}_{\mathrm{T}} = \mathbf{F}_{\mathrm{p}} + \mathbf{F}_{\mathrm{f}} \tag{21}$$

and the drag coefficient of the body is given by

$$C_{\mathrm{D}} = \frac{\mathbf{F}_{\mathrm{T}} \cdot \mathbf{e}_{\mathrm{X}}}{U_\infty^2 a} \tag{22}$$

## 4. NUMERICAL METHOD

The second-order Adams–Bashforth temporal scheme is used together with central differences in space for Equation (11) on a grid defined by $\xi_i = (i-1)\Delta\xi$, $i = 1, 2, \ldots, M$; $\theta_j = (j-1)\Delta\theta$, $j = 1, 2, \ldots, N$; $\Delta\xi = \xi_\infty/(M-1)$ and $\Delta\theta = 2\pi/(N-1)$. The domain is truncated in the $\xi$ direction at $\xi_\infty$. As a result, the calculations of $\omega_{i,j}^{n+1}$ are given by

$$\omega^{n+1} = \omega^n \left(1 + \frac{3}{2}\frac{\Delta t}{a}\frac{\partial f^n}{\partial t}\right) - \omega^{n-1}\left(\frac{\Delta t}{2}\frac{\partial f^{n-1}}{\partial t}\right) + \frac{\Delta t}{2}[3G^n - G^{n-1}] \tag{23}$$

where

$$\begin{aligned} G_{i,j} = {} & \frac{k_i^{-1}\left(\dfrac{\partial k}{\partial \xi}\right)_i^{-1}}{1+f}\left(\left(\frac{\psi_{i,j+1}-\psi_{i,j-1}}{2\Delta\theta} - k(0)\frac{\partial f}{\partial t}\right)\frac{\omega_{i+1,j}-\omega_{i-1,j}}{2\Delta\xi}\right. \\ & \left. - \frac{\psi_{i+1,j}-\psi_{i-1,j}}{2\Delta\xi}\,\frac{\omega_{i,j+1}-\omega_{i,j-1}}{2\Delta\theta}\right) + \frac{\left(\frac{2}{R_{\mathrm{e}}} + \frac{2}{R_{\mathrm{et}}}\right)}{1+f}\left(\left(\frac{\partial k}{\partial \xi}\right)_i^{-2}\right. \\ & \times \frac{\omega_{i-1,j} - 2\omega_{i,j} + \omega_{i+1,j}}{(\Delta\xi)^2} + k_i^{-2}\,\frac{\omega_{i,j-1} - 2\omega_{i,j} + \omega_{i,j+1}}{(\Delta\theta)^2} \\ & \left. + \left(k_i^{-1}\left(\frac{\partial k}{\partial \xi}\right)_i^{-1} - \left(\frac{\partial^2 k}{\partial \xi^2}\right)_i\left(\frac{\partial k}{\partial \xi}\right)_i^{-3}\right)\frac{\omega_{i+1,j}-\omega_{i-1,j}}{2\Delta\xi}\right) \end{aligned} \tag{24}$$

and the superscript $n$ characterizes the time discretization. For the stream function we use a SOR method:

$$\psi_{i,j}^n = \chi\,\frac{S_{i,j}^n - (h_{i,j}^{\mathrm{L}}\psi_{i-1,j}^n + h_{i,j}^{\mathrm{R}}\psi_{i+1,j}^{n-1} + h_{i,j}^{\mathrm{B}}\psi_{i,j-1}^n + h_{i,j}^{\mathrm{T}}\psi_{i,j+1}^{n-1})}{h_{i,j}^{\mathrm{C}}} + (1-\chi)\psi_{i,j}^{n-1} \tag{25}$$

 

where

$$S_{i,j}^{n} = 2\Delta\xi^2\Delta\theta^2\omega_{i,j} \tag{26}$$

$$h_{i,j}^{\mathrm{C}} = -4\left(\Delta\theta^2\left(\frac{\partial k}{\partial\xi}\right)^{-2} + \Delta\xi^2 k^{-2}\right)_{i,j} \tag{27}$$

$$h_{i,j}^{\mathrm{L}} = \Delta\theta^2\left(2\left(\frac{\partial k}{\partial\xi}\right)^{-2} - \Delta\xi\left(k^{-1}\left(\frac{\partial k}{\partial\xi}\right)^{-1} - \left(\frac{\partial^2 k}{\partial\xi^2}\right)\left(\frac{\partial k}{\partial\xi}\right)^{-3}\right)\right)_{i,j} \tag{28}$$

$$h_{i,j}^{\mathrm{R}} = \Delta\theta^2\left(2\left(\frac{\partial k}{\partial\xi}\right)^{-2} + \Delta\xi\left(k^{-1}\left(\frac{\partial k}{\partial\xi}\right)^{-1} - \left(\frac{\partial^2 k}{\partial\xi^2}\right)\left(\frac{\partial k}{\partial\xi}\right)^{-3}\right)\right)_{i,j} \tag{29}$$

$$h_{i,j}^{\mathrm{B}} = h_{i,j}^{\mathrm{T}} = (2\Delta\xi^2 k^{-2})_{i,j} \tag{30}$$

$\chi$ is the over-relaxation parameter and may be taken between 1 and 2. For the downstream boundary condition at infinity, an open boundary condition is established by assuming that the viscous-diffusive effect is negligible and then the vorticity equation is

$$\frac{\partial\omega}{\partial t} - \frac{\omega}{1+f}\frac{\partial f}{\partial t} - \frac{k^{-1}\left(\dfrac{\partial k}{\partial\xi}\right)^{-1}}{1+f}\left[\frac{\partial\omega}{\partial\xi}\left(\frac{\partial\psi}{\partial\theta} - k(0)\frac{\partial f}{\partial t}\right) - \frac{\partial\omega}{\partial\theta}\frac{\partial\psi}{\partial\xi}\right] = 0 \quad \text{for } \xi\to\infty \tag{31}$$

$$\frac{\partial\psi}{\partial\theta} = \frac{1}{2\Delta\theta}(\psi(\xi_\infty,\theta+\Delta\theta) - \psi(\xi_\infty,\theta-\Delta\theta)),$$

$$\frac{\partial\omega}{\partial\theta} = \frac{1}{2\Delta\theta}(\omega(\xi_\infty,\theta+\Delta\theta) - \omega(\xi_\infty,\theta-\Delta\theta))$$

$$\frac{\partial\psi}{\partial\xi} = \frac{1}{\Delta\xi}(\psi(\xi_\infty,\theta) - \psi(\xi_\infty-\Delta\xi,\theta)),$$

$$\frac{\partial\omega}{\partial\xi} = \frac{1}{\Delta\xi}\left(\frac{\omega^{n+1}(\xi_\infty,\theta) + \omega^{n-1}(\xi_\infty,\theta)}{2} - \omega(\xi_\infty-\Delta\xi,\theta)\right)$$

This condition is similar to the so-called 'Radiant Sommerfeld condition'. It remains only to determine the surface vorticity over the cylinder. Equation (12) at $\xi = 0$ is

$$\left(\frac{\partial k}{\partial\xi}(0)\right)^{-2}\frac{\partial^2\psi}{\partial\xi^2} = \omega(0,\theta,t)$$

A Taylor expansion yields a second-order equation for $\omega(0,\theta,t)$ gives,

$$\omega_{1,j} = \frac{\left(\dfrac{\partial k}{\partial\xi}\right)_1^{-2}}{2(\Delta\xi)^2}(-7\psi_{1,j} + 8\psi_{2,j} - \psi_{3,j}) \tag{32}$$

 

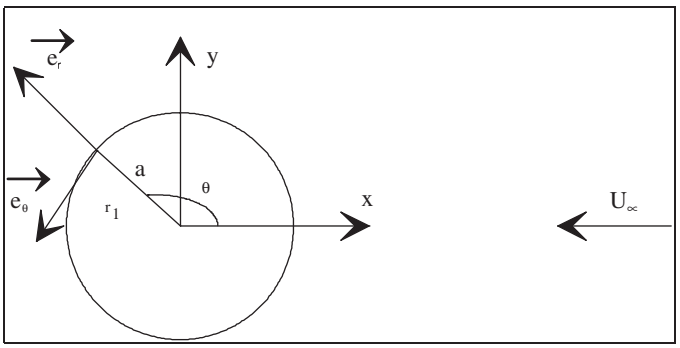


Figure 1. System of co-ordinates.

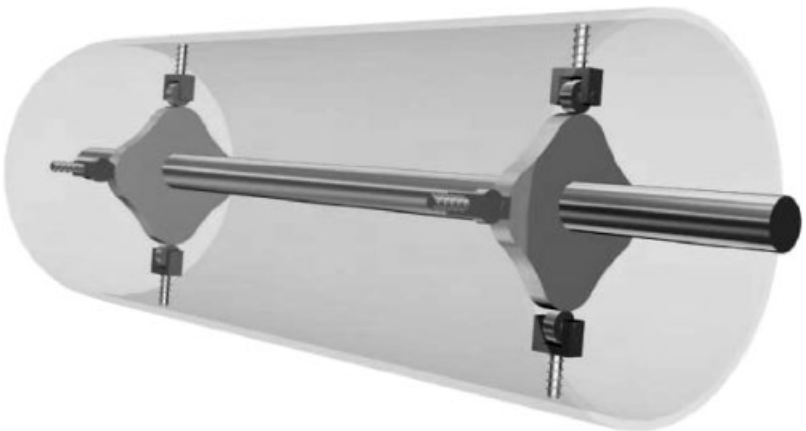

Figure 2. Experimental device.

For the stream function at boundary (for $\xi \to \infty$), after some advances in time, we considered an open boundary condition, i.e. we replaced the condition (17) by

$$\frac{\partial \psi}{\partial \xi} = \frac{1}{\Delta \xi}\left(\frac{\psi_{n+1}(\xi_\infty, \theta) + \psi_{n-1}(\xi_\infty, \theta)}{2} - \psi(\xi_\infty - \Delta\xi, \theta)\right) = 0 \tag{33}$$

or

$$\psi_{n+1}(\xi_\infty, \theta) = 2\psi_n(\xi_\infty - \Delta\xi, \theta) - \psi_{n-1}(\xi_\infty, \theta) \tag{34}$$

## 5. EXPERIMENTAL VALIDATION

For the experimental validation, we used a mechanically deformable cylinder (Figures 1–2).

The experimental device is composed of:

- an electric motor of which the speed of rotation NR can vary, 0 to 300 rpm,

 

- two cams and eight stems transforming rotational movement into radial variation of the cylinder,
- a smoke generator and a camera.

The interval of time between two pictures is $\Delta t_1 = \frac{1}{24}$s. The outer flow velocity is $U_\infty$=2.20m/s. The initial radius of the cylinder is $a_0 = 0.08$ m.

With these data, the initial flow Reynolds number is then $R_{e0} = 2U_\infty a_0/v \approx 23\,500$ and the dimensionless time is $\Delta t = \dfrac{\Delta t_1 U_\infty}{a_0} = 1.15$.

Cams have been designed in a way such that one rotation of the motor correlates to four cycle of the cylinder. So, the dimensionless frequency of deformation is $\Omega = 4\,\mathrm{NR}\, a_0/60U_\infty$. Here, NR is the rotation speed of the motor. We did our experiences for three rotations speeds of the motor: $\mathrm{NR}_1 = 170$ rpm, $\mathrm{NR}_2 = 220$ rpm and $\mathrm{NR}_3 = 300$ rpm, which corresponds to $\Omega_1 = 0.41$, $\Omega_2 = 0.53$ and $\Omega_3 = 0.73$.

## 6. RESULTS FOR $R_{e0} = 23\,500$

We present here the results for the flow at $R_{e0} = 23\,500$. The dimensionless time step is 0.0025, and the grid is 300 divisions in both radial and circumferential directions with the outer boundary at 30 times the diameter of the cylinder. The parameter $C_s$ is chosen to be 0.15 and the parameters $\alpha$ and $\beta$ are chosen to be 0.5. The amplitude of deformation is chosen to be 0.05.

### *6.1. Non-deformable cylinder*

At the beginning of the movement, one notes that a thin primary vorticity layer develops itself all around the cylinder. At $t = 2$, we already see the apparition of two swellings, localized on each side of the downstream stagnation point. These swellings result from the formation of two secondary vortices resulting themselves from the apparition of a reversal flow.

The Reynolds number being important, the primary and secondary vortices are powerful. By the fact of their strength, the secondary vortices develop themselves quickly and push away the primary vortices of the cylinder surface. From $t = 3$, one notes that the secondary vortices penetrate the primary vorticity layer that which feeds the primary vortices and cut these links between $t = 4$ and 5. The primary vortices move away from the cylinder. From $t = 7$, we note the beginning of the primary vortices detachment and the apparition of the Vortex Street.

Thereafter, there is a repetition of these phenomena. Indeed, as leaving of, the primary vortices take a part of secondary vortices. Thus, they lose their strength. Even a new primary vortex takes birth at the same places as that one detached previously. This new pair of primary vortices gives birth to a reversal flow, which will permit the apparition of a new secondary vortex pair, which grows and cuts links between the cylinder and the pair of primary vortex. These are going, again, to detach and to feed the Vortex Street.

At least, we can note the likeness between the experimental visualization and the evolution of the numerical simulation. Indeed, one notes that vortex street appears at the 7th picture for

 

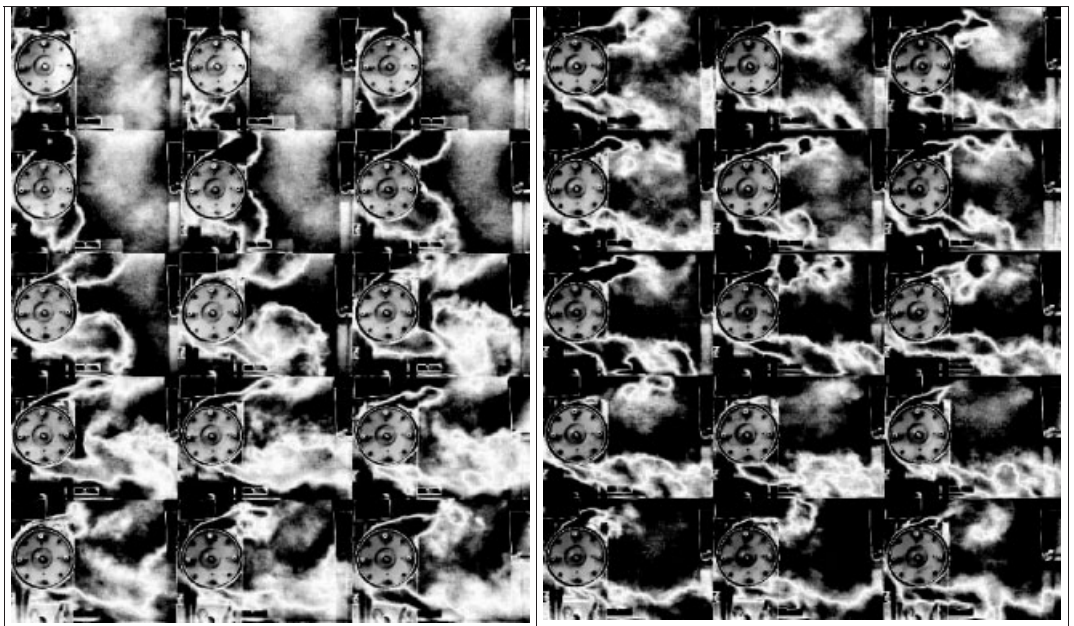

| $t_1 = 0.042$s to $t_1 = 0.625$s | $t_1 = 0.667$s to $t_1 = 1.250$s |
|---|---|

Figure 3. Experimental visualization of the evolution of the streamlines for a non-deformable cylinder.

the experimental visualization (Figures 3 and 4). The interval of time between two pictures being $\frac{1}{24}$ of second, it occurs at $t_1 = 0.3$ s. It corresponds to the non-dimensional time $t = 8.25$. It reconfirmed again approximately the numerical simulation results, where one can see that at $t = 8$, primary vortex, localized at the intrados, begins to detach (Figures 5 and 4).

Besides, we notice that the primary vorticity layer spreads in the near wake of the cylinder. This phenomenon is found, again, as well in the pictures of the experimental visualization as by the results of the numerical simulation (Figures 3, 5 and 6).

For the drag coefficient, we note an oscillation of values at the beginning of the simulation (see Figure 7). Values of the $C_D$ fluctuate between $-2$ and 2. This oscillation attenuates itself during this time and stabilizes from $t = 12$ about the value of $C_D = 0.4$.

### 6.2. *Deformable cylinder*

*6.2.1.* $\Omega_1 = 0.41$. The vibration of the cylinder radius modifies appreciably the structure of the flow around it.

Throbbing, transmitted by the cylinder to the fluid that surrounds it, creates a secondary flow that attracts the flow toward the cylinder when this one retracts and repulses it when the cylinder dilates (Figure 8). This secondary flow plays an important role in the evolution of the flow structure. We note that the formation and the detachment of primary vortices

 

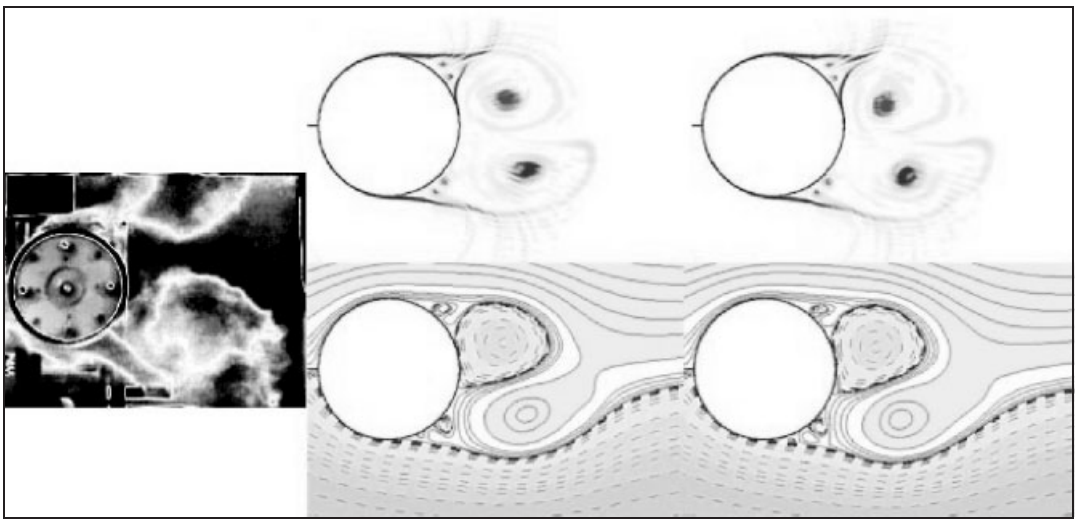


Figure 4. Comparison between experimental visualization and numerical simulation (detachment of the intrados vortex).

are accelerated. Indeed, the secondary flow gives more strength to the secondary vortices and permits them to cut more quickly the links between the primary vorticity layer and the primary vortices (see Figure 9). The primary vortices are less powerful and smaller than those we had for the flow around a non-deformable cylinder. But one notes that, contrary to non-deformable case, the first primary vortex pair is not able to move away from the cylinder, which attracts it toward its surface when it retracts (Figure 10, $t = 4$). The second primary vortex pair, that is already formed and detached, reaches up the first one, merges with it and forms a more powerful pair of primary vortex (Figure 10, $t = 5$–$7$). We see, then, that the third primary vortices pair is accelerated by the secondary flow and reaches up the first two pairs already merged (Figure 10, $t = 8$ and 9). This primary vortex pair, which becomes very powerful, can resist the cylinder attraction and moves away while spreading in the wake (Figure 10, $t = 10$). We note, thereafter, some regularity in the primary vortices formation and detachment. This periodicity is equal to $t = 2.5$, that is to say the frequency $f = 0.4$. This frequency is nearly the same as that of the cylinder radius deformation. Therefore, we can say that the cylinder captured the Vortex Street frequency (Figure 10).

We note that the concordance of the numerical simulation results and the experimental visualization is very satisfactory. So, we can note that at $t_1 = 0.17$ s, which corresponds to $t = 4.67$ (Figure 11), there are two primary vortex pairs attached to the cylinder (figure gives flow streamlines comparing the experimental visualization). There exists a small dissymmetry in the experimental visualization, which is surely owed to experimentation conditions. At $t_1 = 0.75$ s, which corresponds to $t = 20.63$ (Figure 12), we see, first of all, some deviation of flow downwards as well for numerical simulation as for the experimental visualization. We can also notice some similarities existing between the experimental visualization and the

 

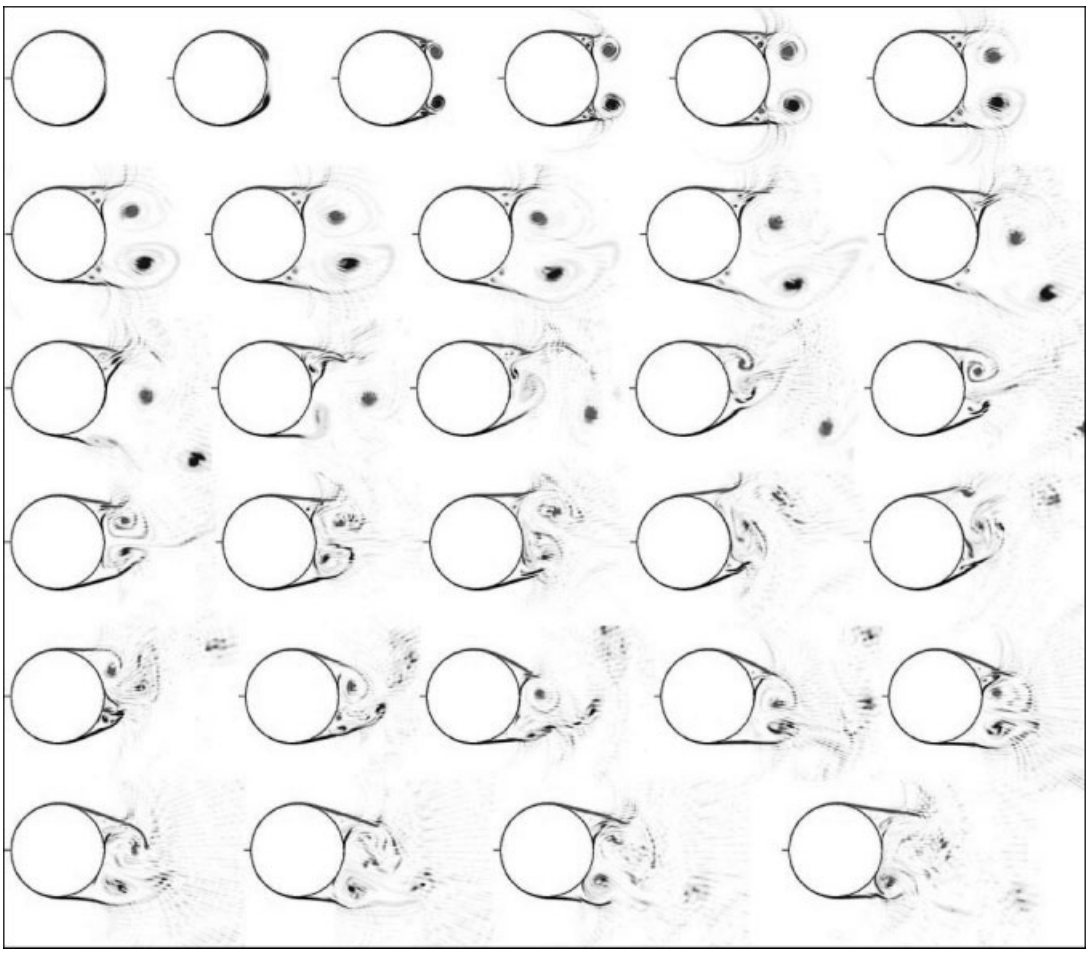

Figure 5. Numerical visualization of the vorticity for a non-deformable cylinder ($t = 1$–$30$).

numerical simulation concerning the vortices dispositions (the same happens for $t_1 = 1$ s, that corresponds to $t = 27.5$ (Figure 13), except the fact that the wake is now become powerful and horizontal).

The increase of the cylinder diameter is characterized by the creation of a secondary flow (Figure 8), which, on the rear part of the cylinder, has tendency to propel the cylinder [3]. This phenomenon has some favourable repercussions on the evolution of the drag coefficient [3].

We made to coincide, in the numerical simulation, the impulsive start of the movement with an increase of diameter of the first oscillation cycle. When the wall deformation velocity becomes maximum, the strength of the secondary flow is, then, maximum. The strength of propulsion force created by the cylinder, as it is expelling the fluid of the secondary flow rearward, is the most intense. This force is to be added to effects of the impulsive starting.

 

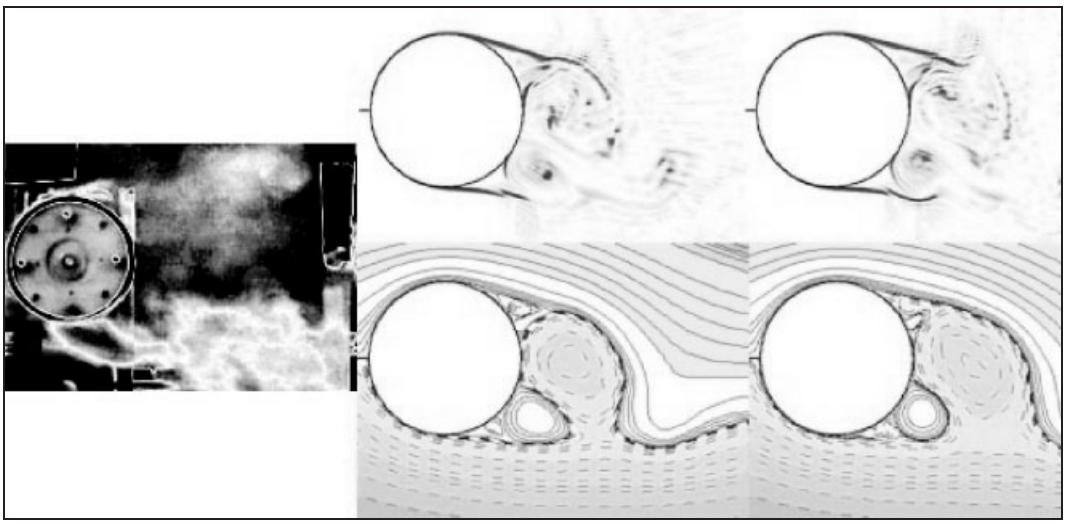

$t_1 = 1.042s$ t = 28.5 t = 29

Figure 6. Comparison between experimental visualization and numerical simulation (primary vorticity layer spreads in the near wake of the cylinder).

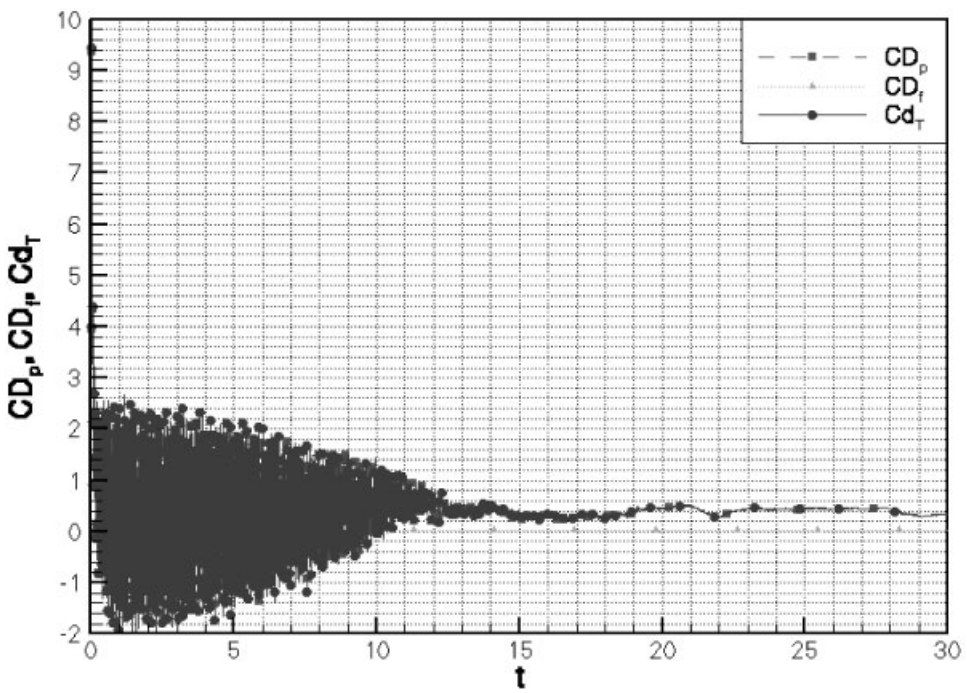


Figure 7. Evolution of the drag coefficient for a non-deformable cylinder.

 

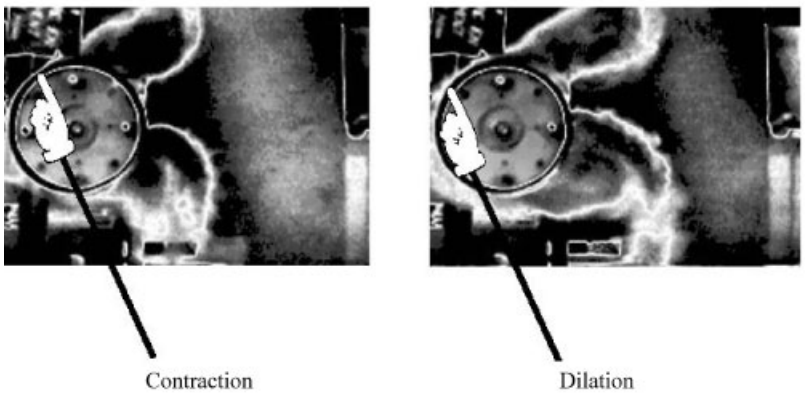


Figure 8. Effect of the radius vibration on the primary vorticity layer (creation of secondary flow).

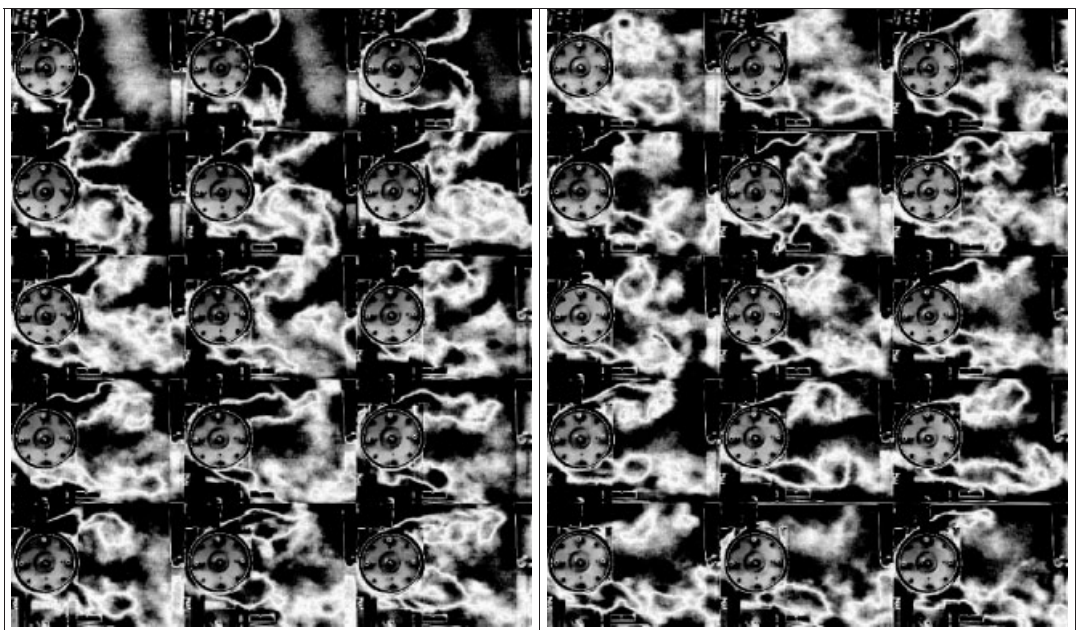


Figure 9. Experimental visualization of the evolution of the streamlines for a deformable cylinder ($\Omega = 0.41$).

The drag coefficient decreases (Figure 14). Unfortunately, the more one brings closer to $t = 0.625$, more slow is the wall deformation velocity. The intensity of the propulsion force, created by the cylinder, decrease. Besides, we see the beginning of the development of the primary vorticity layer (Figure 10). Therefore, there is the reduction of the drag coefficient

 

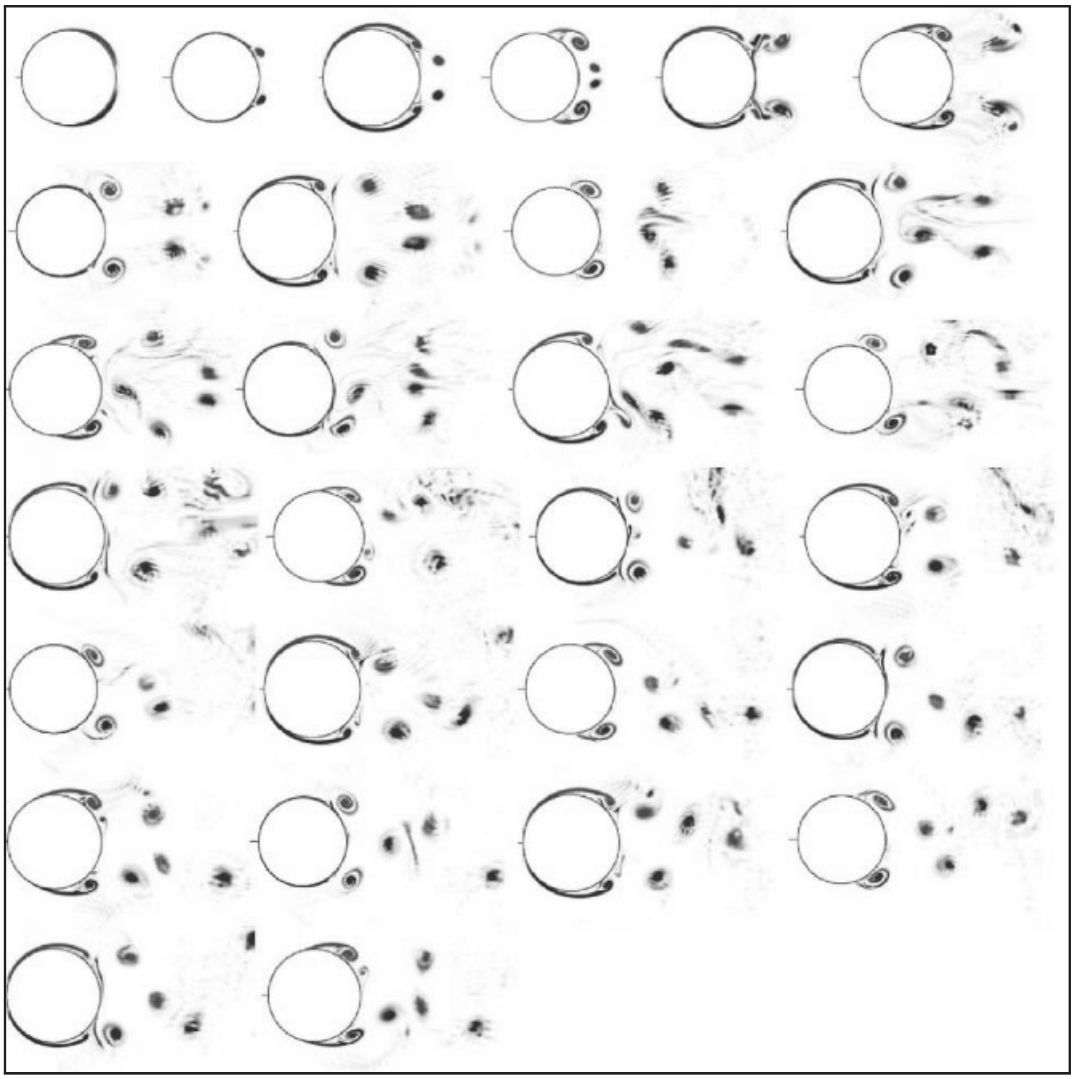

Figure 10. Numerical visualization of the vorticity for a deformable cylinder ($t = 1$–$30$).

slope between $t = 0.5$ and 0.625. From $t = 0.625$, the cylinder diameter decreases, with a wall deformation velocity that increases to reach its maximal value at $t = 1.25$. During this quarter of period, the cylinder attracts the fluid. Approaching to $t = 1.25$, the cylinder attracting velocity increases. In the rear part of the cylinder, the outer fluid flow, attracted by the cylinder, comes to strike it and propels it forwards [4]. The drag coefficient decreases more quickly and reaches some negative values (Figure 14). The cylinder is propelled. Between $t = 1.25$ and 1.875, the cylinder diameter continues to decrease, but with a wall deformation velocity that decreases until it reaches zero for $t = 1.875$. The strength of attracting, exercised by the cylinder on the fluid flow, decreases. The strength with which this outer fluid flow comes

 

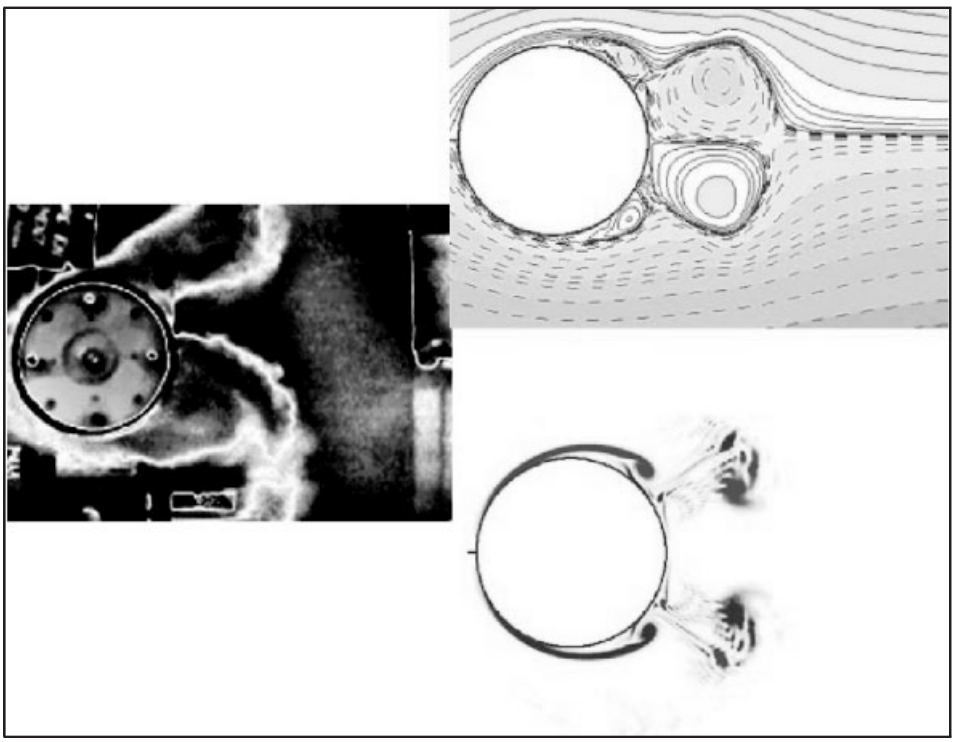

Figure 11. Comparison between experimental visualization and numerical simulation ($t_1 = 0.17$ s which correspond to $t = 5$).

to hit the rear of the cylinder decreases until it annuls. Besides, we note a primary vortices development, which remain attached to the cylinder (Figure 10). The drag coefficient increases and reaches some positive values (Figure 14). The cylinder is braked. From $t = 1.875$, the cylinder diameter restarts to increase with a wall deformation velocity that increases to reach its maximum at $t = 2.5$. The secondary flow reappears. More one advances in time, more powerful is this secondary flow. The secondary flow permits to increase the secondary vortices strength which arrive to cut links between the primary vortices and the cylinder at $t = 2$. The drag coefficient restarts to decrease (Figure 14).

Then, we note a repetition of phenomena we have just described (Figure 14). Indeed, the drag coefficient evolution in time becomes periodic and of the same period as that of the cylinder deformation (Figure 10). One can also see that the negative part is more important than the positive part for every period. It means that the cylinder deformation can have some favourable effects for the propulsion of the cylinder.

*6.2.2.* $\Omega_2 = 0.53$. For this wall deformation frequency, we have the same phenomena (Figure 15) as those we described in the previous case (Figure 10). Indeed, all phenomena described previously are present again. The only differences come from the fact that the

 

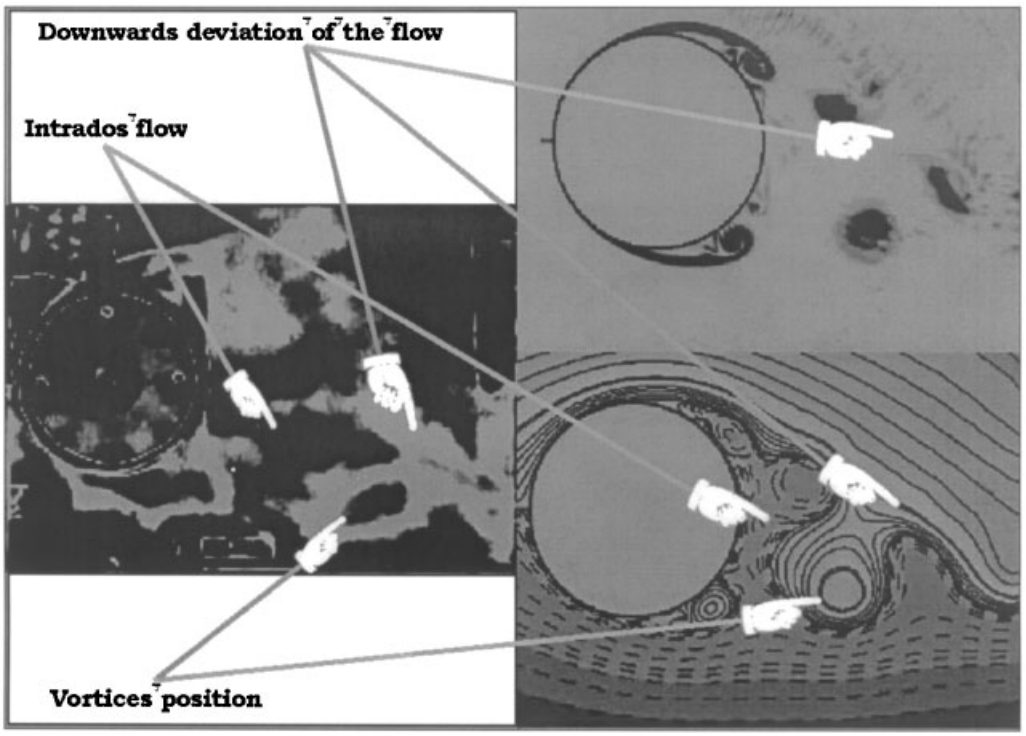


Figure 12. Comparison between experimental visualization and numerical simulation ($\Omega = 0.41$, $t_1 = 0.75$ s which correspond to $t = 20.5$).

wall deformation frequency being higher, phenomena occur more quickly (Figure 15). So, the period of primary vortices detachment, in this case, is equal to $T = 1.85$ that correspond to a frequency $\Omega = 0.54$ (Figure 15). This frequency is the one of the cylinder wall deformation. The second difference is that the wall deformation frequency being higher, the strength with which the cylinder pushes the secondary flow and the primary vortices is more powerful. We remark that the cylinder pushes away the primary vortices so far that they move away a distance from where they are not brought back to the surface and do not merge anymore to form some more powerful vortices. So a multitude of small vortices, which flow out in the wake, appears (Figure 15).

Comparing the experimental visualization (Figure 16) and the numerical simulation (Figure 15), we note a good concordance in the apparition of different phenomena and in the wake structure (Figures 17–19).

Concerning the drag coefficient we can note the same effects as those found previously (Figure 20). The only two differences are that the strengths of attraction and repulsion of the cylinder being more important, the minimal and maximal values of the drag coefficient are bigger (Figure 20) than those in the previous case (Figure 14). The second difference is that the period of phenomenon repetition is, in this case, equal to $T = 1.85$. It is the same as the cylinder wall deformation period.

 

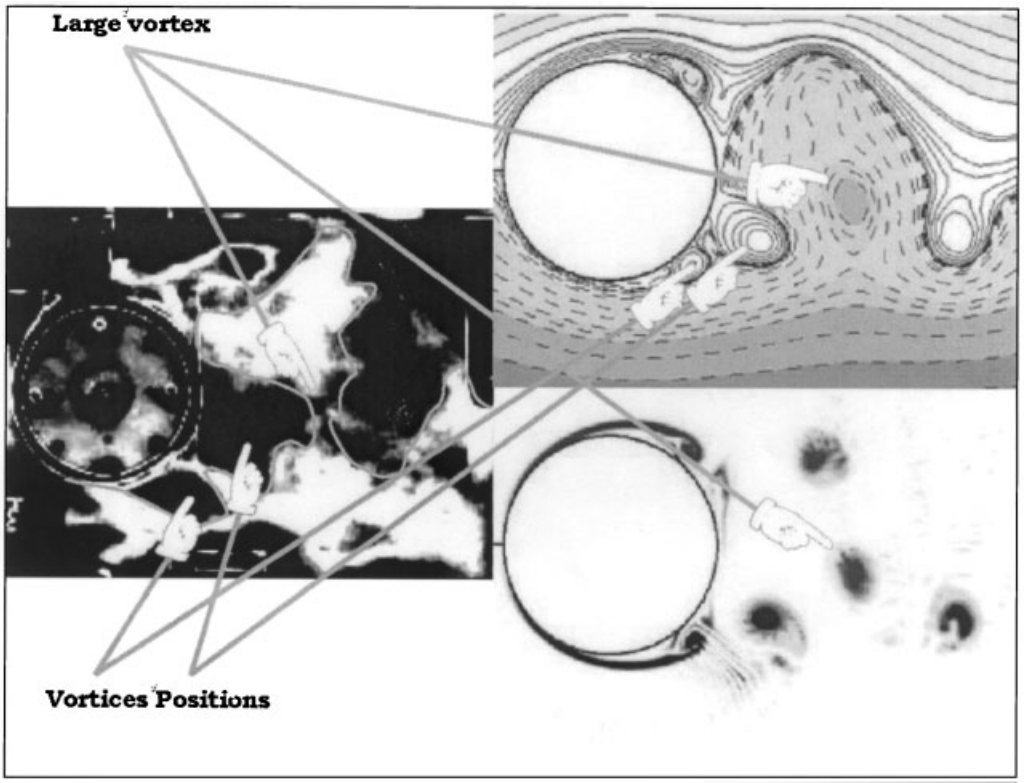


Figure 13. Comparison between experimental visualization and numerical simulation ($\Omega = 0.41$, $t_1 = 1$ s which correspond to $t = 27.5$).

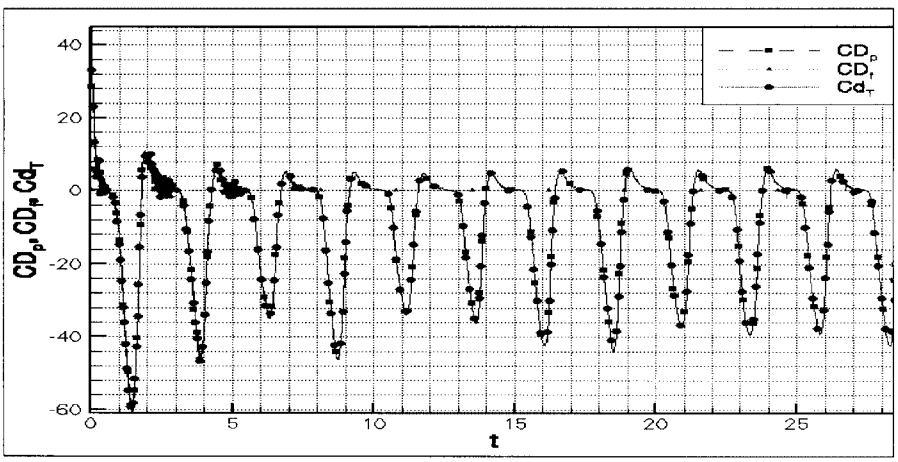


Figure 14. Evolution of the drag coefficient for a deformable cylinder ($\Omega = 0.41$).

 

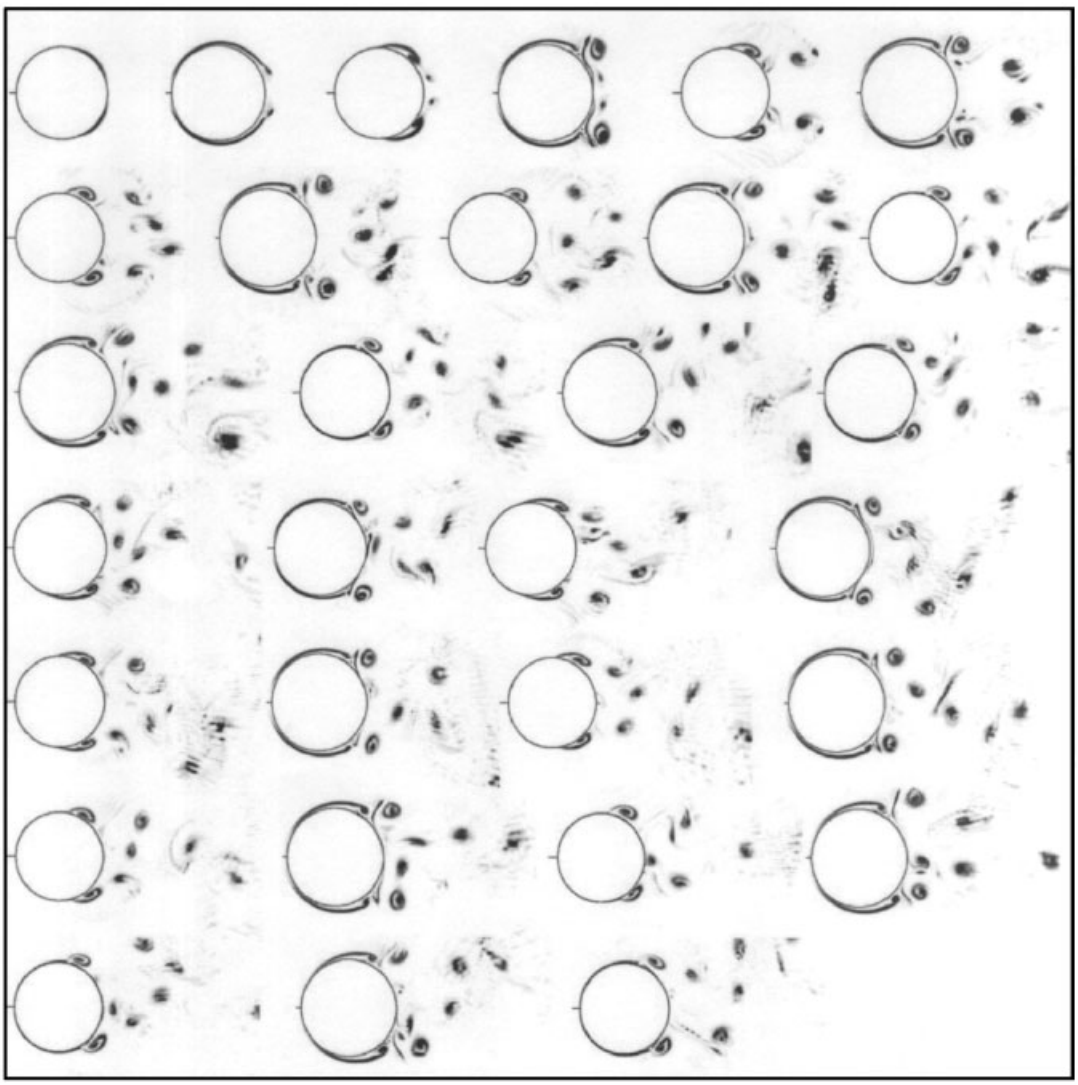

Figure 15. Numerical visualization of the vorticity for a deformable cylinder ($t = 1$–$30$).

*6.2.3.* $\Omega_3 = 0.73$. For this wall deformation frequency, we note that the flow structure differs slightly (Figure 21) from that for $\Omega = 0.43$ (Figure 15). The secondary flow emanating from the cylinder, when this one is in extension, is more powerful. In the same way, the attraction that it exercises on the downstream fluid is more powerful. The formation and detachment process of primary vortices pair is still the same (Figure 21). The difference, here, comes from the fact that the detached primary vortex pair is propelled far downstream the cylinder (Figure 21). It loses, then, its velocity when the cylinder begins to attract the fluid of the downstream flow. It reaches up and exceeds by the second pair, which is formed and detached.

 

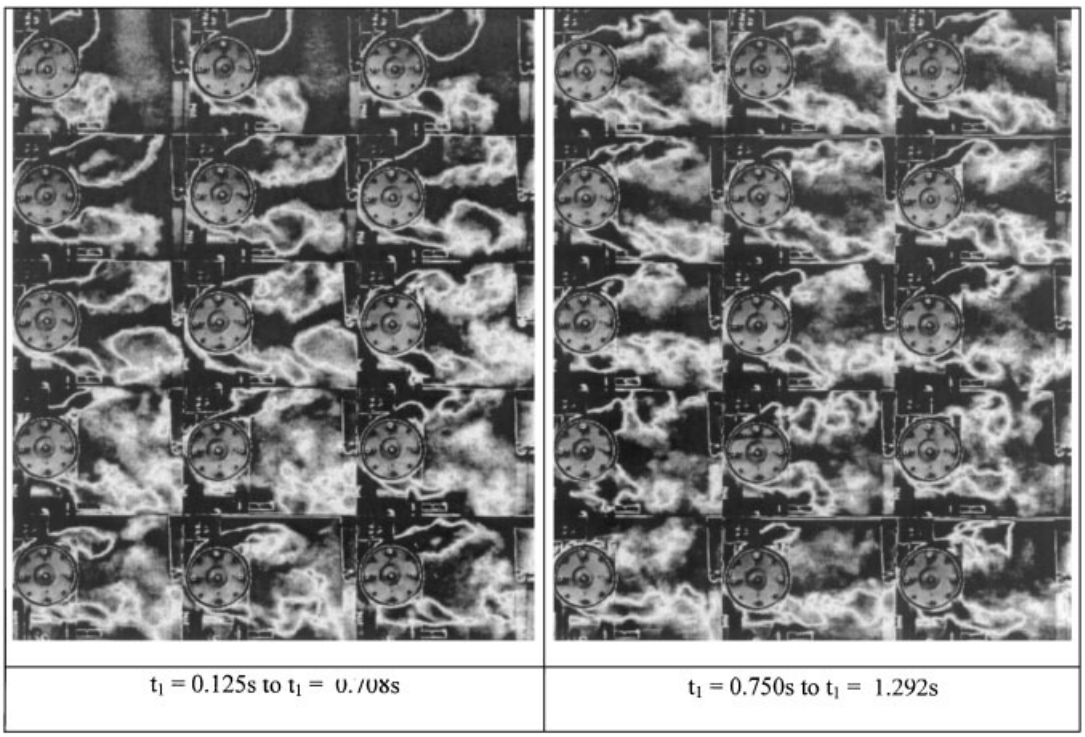


Figure 16. Experimental visualization of the evolution of the stream lines for a deformable cylinder.

Indeed, this new pair being closer to the cylinder, is propelled by a more important strength. Besides, the intrados vortices (as well as extrados vortices) rotating in the same direction, the emanating vortex of the second primary vortices pair, pushes the emanating vortex of the first pair towards the cylinder (Figure 21). Thereafter, one can see that the third primary vortex pair is formed and detached, and benefits, in addition to the propulsion due to the cylinder, from the presence of the two previous pairs of primary vortices to escape quickly from the attraction of the cylinder (Figure 21). Then, these vortices lose their velocities and some of them merge to form some more powerful vortices. They can escape completely from the attraction of the cylinder and form the vortex street. One notes that the frequency of primary vortices detachment is equal to the wall deformation frequency. So, the period of primary vortices detachment is $T = 1.35$, which corresponds to a frequency of $\Omega = 0.74$.

It shows, once again, that the cylinder captures the frequency of primary vortices detachment, confirming, thus, the 'lock-in' process.

In this case, also, the comparison between the experimental visualization (Figure 22) and the numerical simulation (Figure 21), are in good concordance concerning the apparition of the phenomena as well as the wake structure (Figures 23–25).

The experimental visualization (Figure 23) shows that there are two vortices (on the intrados and on the extrados): one attached to the cylinder and the other one slightly distant from the cylinder. We note, on the other hand, that they are more distant from the downstream

 

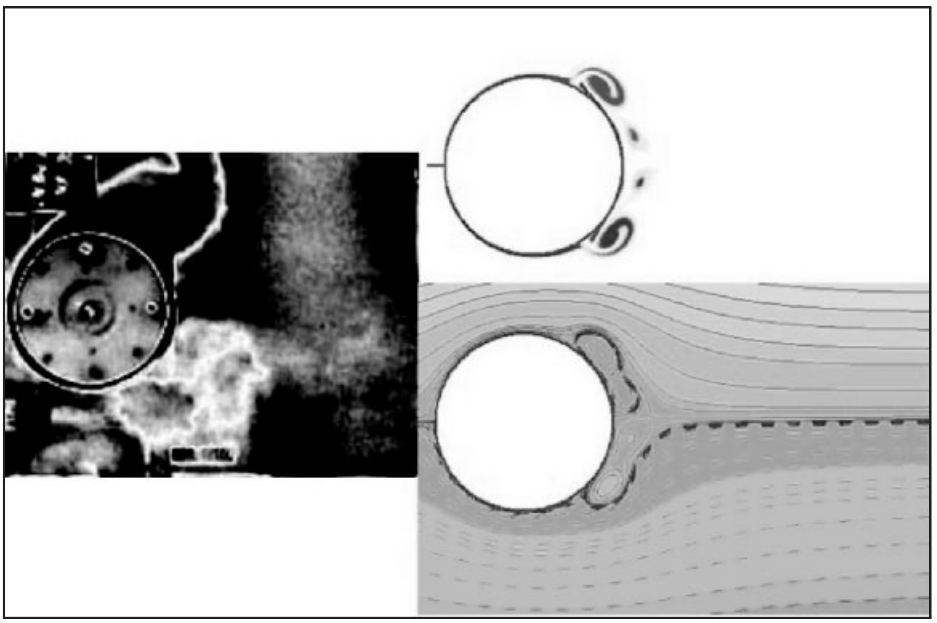

Figure 17. Comparison between experimental visualization and numerical simulation ($\Omega = 0.53$, $t_1 = 0.125$ s which correspond to $t = 3.5$).

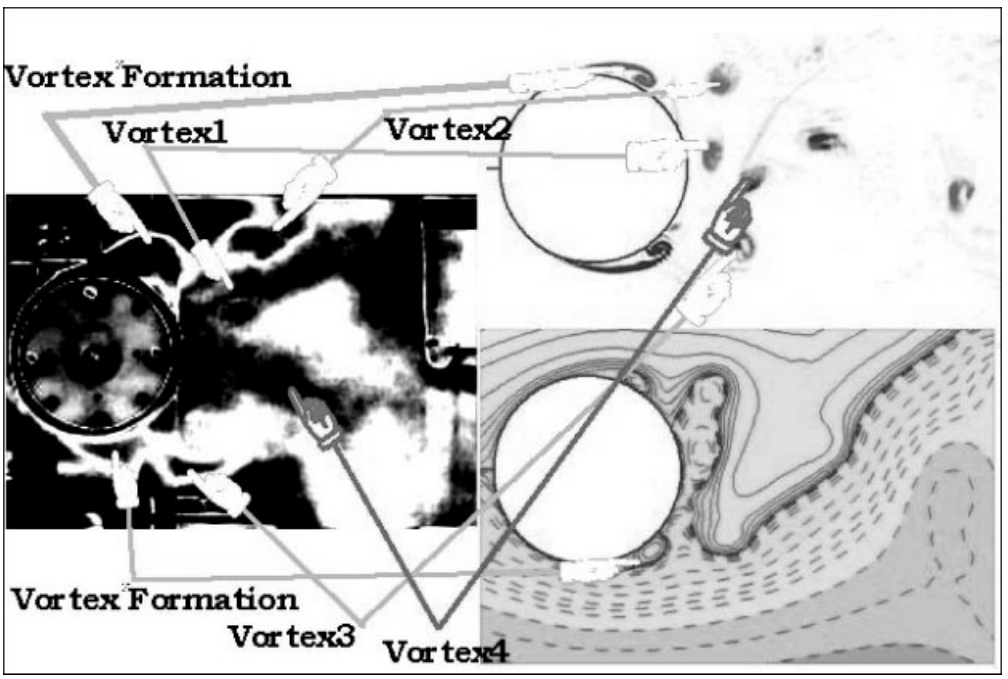


Figure 18. Comparison between experimental visualization and numerical simulation ($\Omega = 0.53$, $t_1 = 0.583$ s which correspond to $t = 16$).

 

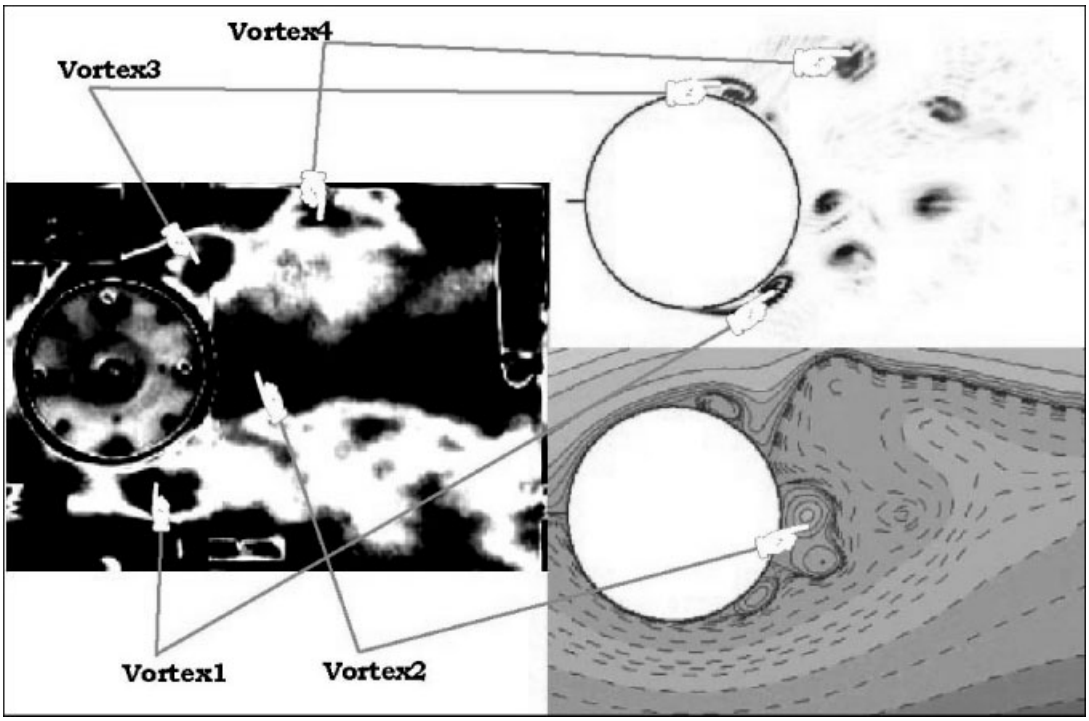


Figure 19. Comparison between experimental visualization and numerical simulation ($\Omega = 0.53$, $t_1 = 1$ s which correspond to $t = 27.5$).

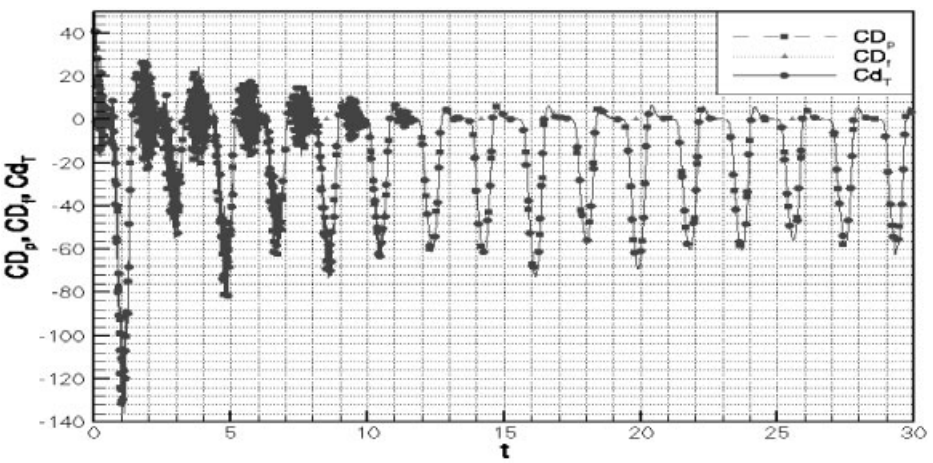


Figure 20. Evolution of the drag coefficient for a deformable cylinder ($\Omega = 0.53$).

 

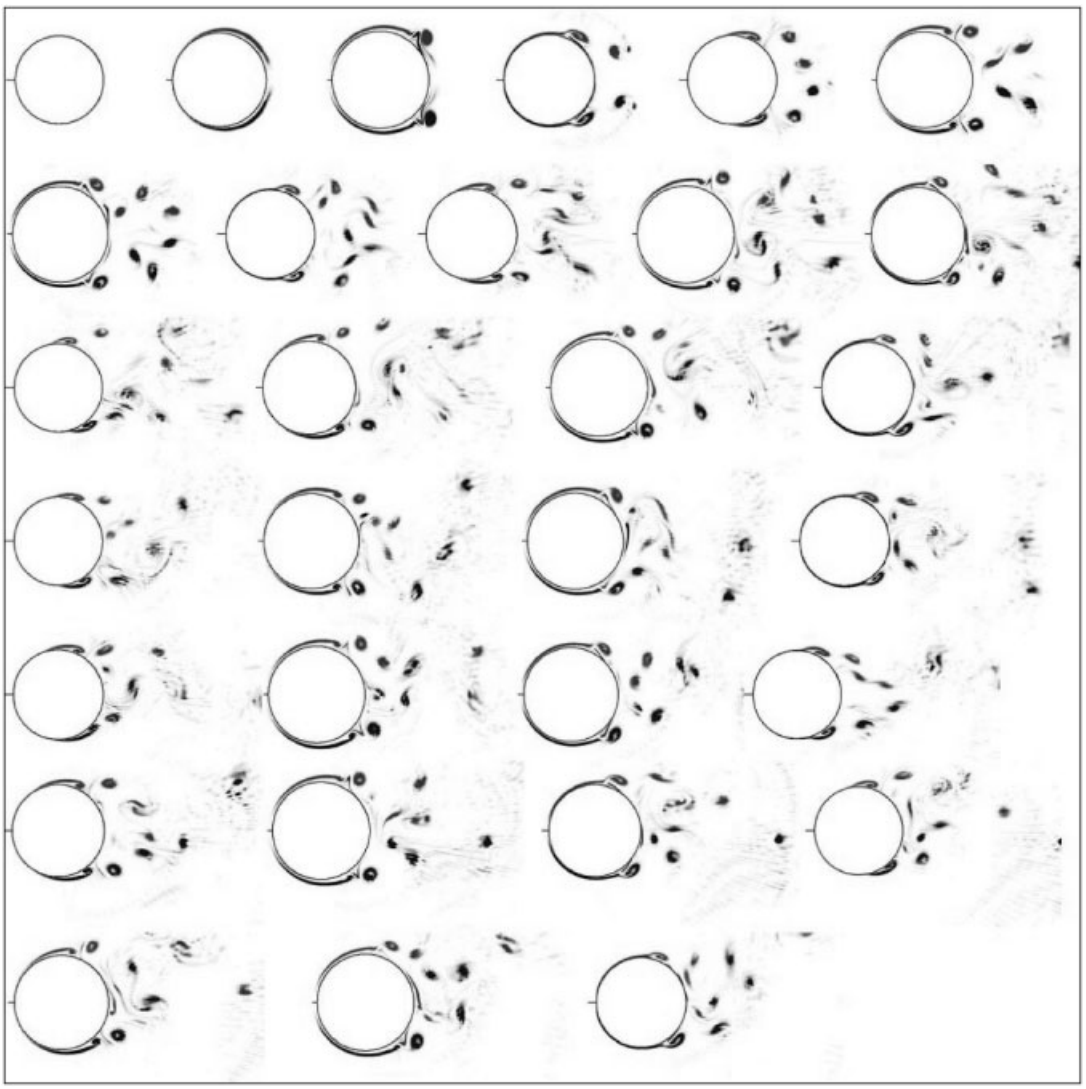

Figure 21. Numerical visualization of the vorticity for a deformable cylinder ($t = 1$–$30$).

symmetry axis of the cylinder. We think that this difference is due to experimental conditions, which are not so perfect as those of the numerical simulation.

In the second comparison (Figure 24), we see that there exists similarity in the experimental visualization and the numerical simulation. Indeed, we see the primary vorticity layer length down behind the cylinder and the small primary vortices situated behind the cylinder. We also note, in the middle, behind the cylinder, the presence of a large vortex which results from the presence of the three small primary vortices turning in sense, visible on the numerical simulation.

 

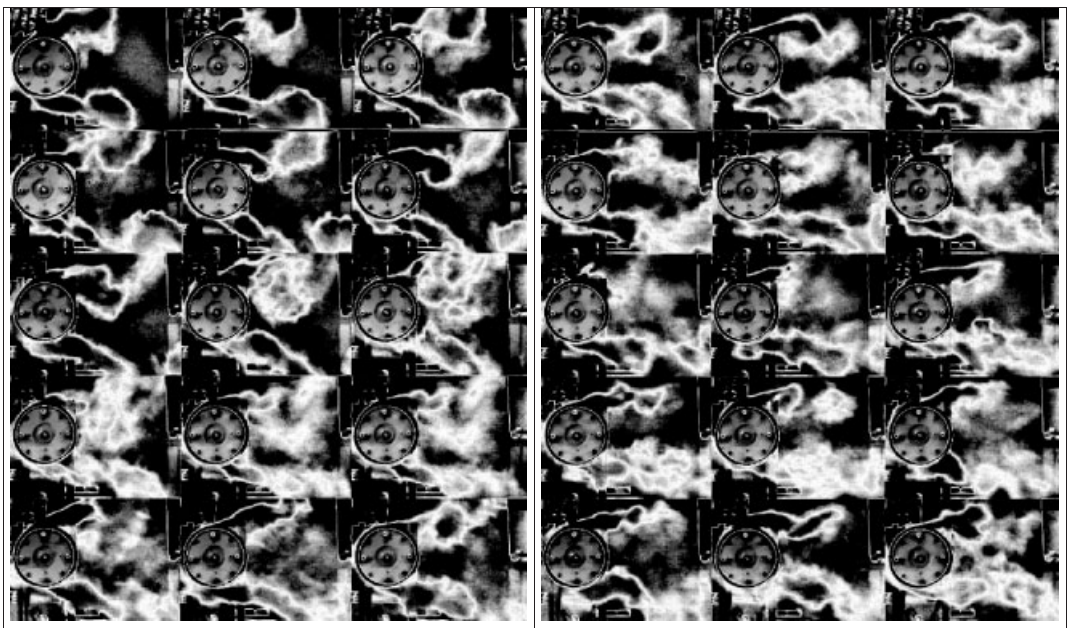

| $t_1 = 0.167s$ to $t_1 = 0.750s$ | $t_1 = 0.792s$ to $t_1 = 1.375s$ |
|---|---|

Figure 22. Experimental visualization of the evolution of the stream lines for a deformable cylinder.

In the last comparison (Figure 25), we see that the three small primary vortices, turning in the same direction, are very close to the wall cylinder. It is visible in the two cases (numerical and experimental). Evidently, the primary vorticity layer on the extrados is blocked by a big vortex (formed by the three ones turning in the same direction). On the other hand, on the intrados, it extends behind the cylinder.

Regarding the drag coefficient we can also note the same effects as those found previously (Figure 26). There are only two differences: (1) the strengths of attraction and repulsion of the cylinder being more important, the minimal and maximal values of the drag coefficient are bigger (Figure 26) compared to those obtained in the previous case (Figures 14 and 20). (2) The period of phenomenon repetition is, in this case, equal to $t = 1.35$, the same as the cylinder wall deformation frequency.

## 7. CONCLUSION

The present numerical simulation and experimental visualization concern the analysis of unsteady separated flow and 'lock-in' phenomenon around the impulsively starting deforming cylinder for the Reynolds number $R_{e0} = 23\,500$. Firstly, all the results, including the $\beta$-phenomenon, previously detected either numerically or by experiment visualization [5, 6], have been reproduced in detail in the preliminary non-deformable case.

 

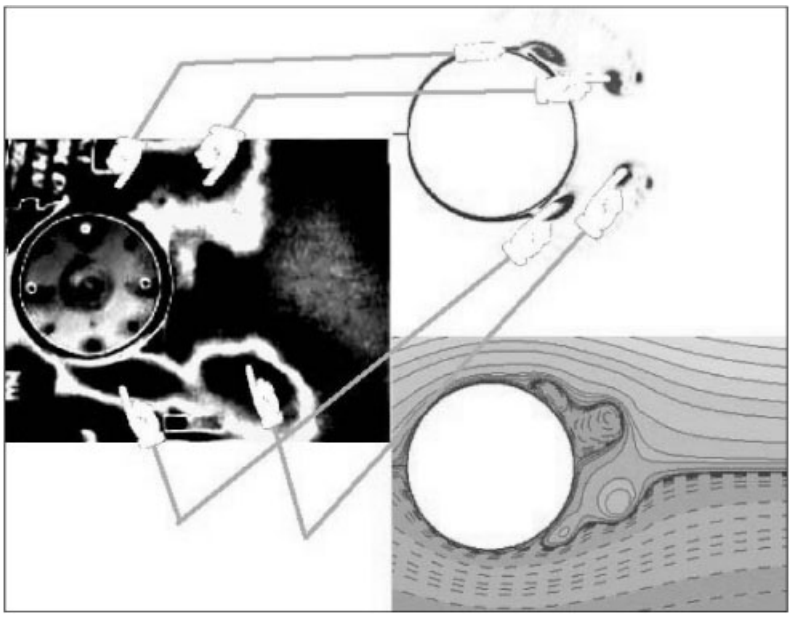

Figure 23. Comparison between experimental visualization and numerical simulation ($\Omega = 0.73$, $t_1 = 0.167$ s which correspond to $t = 4$).

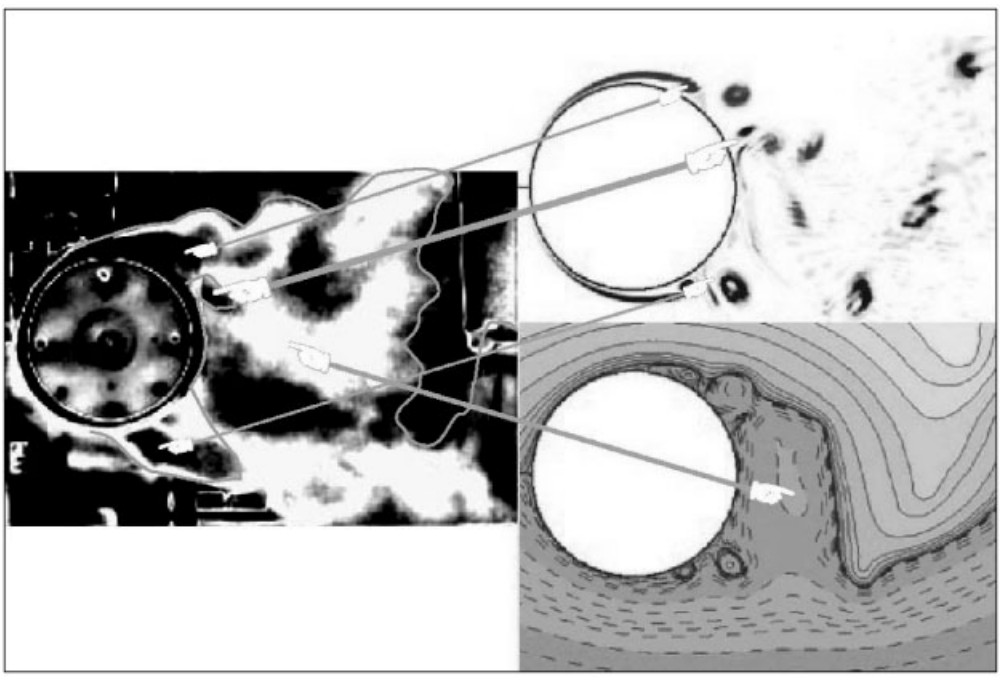

Figure 24. Comparison between experimental visualization and numerical simulation ($t_1 = 0.625$ s which correspond to $t = 17$).

 

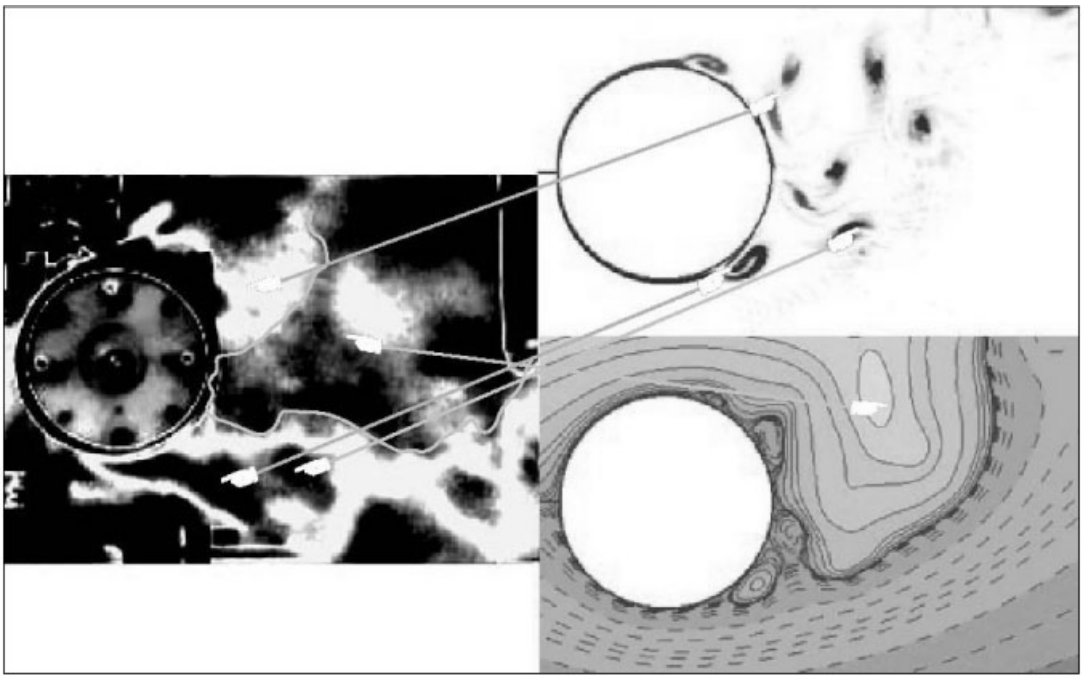

Figure 25. Comparison between experimental visualization and numerical simulation ($\Omega = 0.73$, $t_1 = 1.083$ s which correspond to $t = 30$).

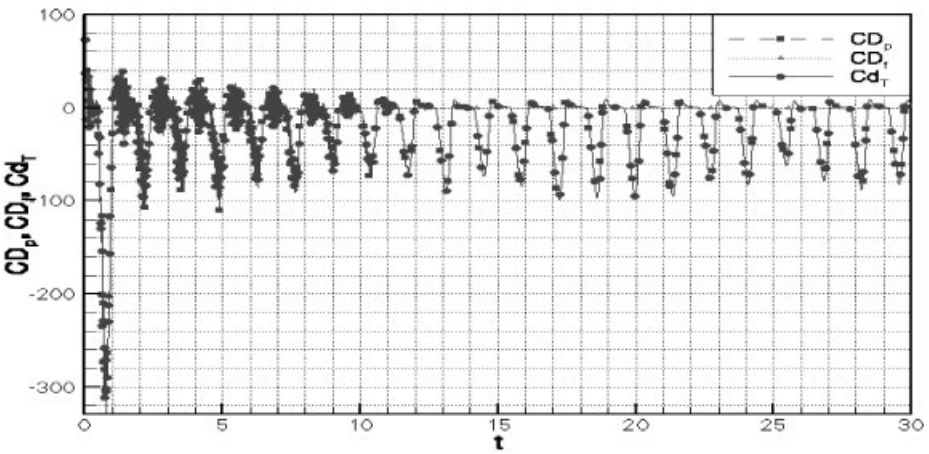


Figure 26. Evolution of the drag coefficient for a deformable cylinder ($\Omega = 0.73$).

 

We showed that the wall deformation created a secondary radial flow at the neighbourhood of the surface cylinder [4, 7]. This secondary flow plays a very important role in the wake structure. Indeed, this secondary flow permits to cut links between the cylinder and the primary vortices quickly. It permits also to form Vortex Street more quickly, modifying the wake structure considerably. We show that the wall deformation frequency influences the vortex detachment frequency. So, the frequency of primary vortex detachment becomes equal to the wall deformation frequency. This synchronization phenomenon, often called 'lock-in', may cause undesirable effects, but may also constitute a way of controlling the wake development. We show, also, that the cylinder wall deformation influences the evolution of the drag coefficient. Indeed, the variation of the drag coefficient becomes periodic and of the same frequency as the one of the wall deformation. An increase of the diameter has similar effects as an injection of fluid on the entire cylinder surface, whereas a reduction of diameter of diameter has some similar effects as suction on the entire cylinder surface [4]. In the growing phase, the greater the frequency deformation of the cylinder, the more important the force of propulsion created by the cylinder pushing the flow outwards. So, the drag coefficient decreases. In retraction phase, the cylinder attracts the fluid of the outer flow. The greater the deformation frequency, the bigger the attractive force in the rear part of the cylinder. So, the free outer fluid flow, attracted by the cylinder, comes to strike it and propel it forwards. The drag coefficient decreases and reaches some negative values. The cylinder is propelled.

So, body deformability may be used as wake control device that would favourably affect the interplay of primary and secondary vorticity, thus reducing the drag coefficient. We are trying now to show that all that we found for this Reynolds number is valid for other bigger Reynolds numbers. We are just achieving experimentations for Reynolds numbers from 100 000 to 5 000 000 with 'PIV' techniques and confronting them with results of the numerical simulation.

## REFERENCES

1. Zhang J, Dalton C. Interaction of vortex-induced vibrations of a circular cylinder and steady approach flow at Reynolds number of 13000. *Journal of Computer and Fluid* 1996; **45**:283–294.
2. Coutanceau M, Defay JR. Circular cylinder wake configuration: a flow visualization survey. *Applied Mechanics Reviews* 1991; **44**(6):255–305.
3. Koopmann GH. The vortex wakes of vibrating cylinders at low Reynolds numbers. *Journal of Fluid Mechanics* 1967; **28**:501–512.
4. Hanchi S, Askovic R, Ta Phuoc L. Numerical simulation of flow around an impulsively started radially deforming circular cylinder. *International Journal for Numerical Methods in Fluids* 1999; **29**:555–573.
5. Koumoutsakos P, Leonard A. High-resolution simulations of the flow around an impulsively started cylinder using vortex method. *Journal of Fluid Mechanics* 1995; **196**:1–38.
6. Bouard R, Coutanceau M. Etude expérimentale de l'écoulement engendré par un cylindre en translation dans un fluide visqueux en régime de Stokes. *Journal of Fluid Mechanics* 1986; **37**:673–684.
7. Hanchi S, Askovic R. Approche numérique du transfert thermique convectif pour un cylindre circulaire déformable. *International Journal of Heat and Mass Transfer* 1998; **41**(11):1385–1396.

 